

A MULTIWAVELENGTH STUDY OF YOUNG MASSIVE STAR-FORMING REGIONS. III. MID-INFRARED EMISSION

ESTEBAN F. E. MORALES¹, DIEGO MARDONES AND GUIDO GARAY
Departamento de Astronomía, Universidad de Chile, Casilla 36-D, Santiago, Chile

KATE J. BROOKS²
Australia Telescope National Facility, P.O. Box 76, Epping NSW 1710, Australia

AND

JAIME E. PINEDA²
Harvard-Smithsonian Center for Astrophysics, 60 Garden Street, MS-10, Cambridge, MA 02138
Published in ApJ, 698, 488

ABSTRACT

We present mid-infrared (MIR) observations, made with the TIMMI2 camera on the ESO 3.6 m telescope, toward 14 young massive star-forming regions. All regions were imaged in the *N* band, and nine in the *Q* band, with an angular resolution of $\simeq 1''$. Typically, the regions exhibit a single or two compact sources (with sizes in the range 0.008–0.18 pc) plus extended diffuse emission. The *Spitzer*–Galactic Legacy Infrared Mid-Plane Survey Extraordinaire images of these regions show much more extended emission than that seen by TIMMI2, and this is attributed to polycyclic aromatic hydrocarbon (PAH) bands. For the MIR sources associated with radio continuum radiation (Paper I) there is a close morphological correspondence between the two emissions, suggesting that the ionized gas (radio source) and hot dust (MIR source) coexist inside the H II region. We found five MIR compact sources which are not associated with radio continuum emission, and are thus prime candidates for hosting young massive protostars. In particular, objects IRAS 14593–5852 II (*only* detected at 17.7 μm) and 17008–4040 I are likely to be genuine O-type protostellar objects. We also present TIMMI2 *N*-band spectra of 8 sources, all of which are dominated by a prominent silicate absorption feature ($\simeq 9.7 \mu\text{m}$). From these data we estimate column densities in the range $(7–17) \times 10^{22} \text{ cm}^{-2}$, in good agreement with those derived from the 1.2 mm data (Paper II). Seven sources show bright [Ne II] line emission, as expected from ionized gas regions. Only IRAS 12383–6128 shows detectable PAH emission at 8.6 and 11.3 μm .

Subject headings: dust, extinction — infrared: ISM — stars: early-type — stars: formation

1. INTRODUCTION

Massive stars are known to be born deeply embedded within dense clumps of molecular gas and dust, with distinctive physical parameters: sizes of $\simeq 0.4$ pc, masses of $\simeq 5 \times 10^3 M_{\odot}$, and dust temperatures of $\simeq 32$ K (e.g., Faúndez et al. 2004). The formation process of massive stars within these clumps is, however, still under discussion. Current theories are coalescence (e.g., Bonnell et al. 1998; Bonnell & Bate 2002), gravitational collapse of single massive prestellar cores (e.g., McKee & Tan 2003; Krumholz et al. 2007), and competitive accretion (e.g., Bonnell et al. 2004). At least up to masses corresponding to late O-type stars and early B-type stars, the observational evidence of accretion disks and molecular outflows favors the collapse scenario (see the reviews by Garay & Lizano 1999; Beuther et al. 2007). The observational study of the early stages of high-mass stars is difficult because of three main reasons: the rapid pre-main-sequence evolution of massive stars, confusion problems for individual studies since they form in clusters and are located at longer distances than low-mass stars, and the large columns of dust and gas ($N(\text{H}_2) \simeq 3 \times 10^{23} \text{ cm}^{-2}$, Garay et al. 2007) of the dense molecular clouds that harbor them, making them com-

pletely dark at visual wavelengths. Thus, the study of the environment around recently formed massive stars is better performed through observations at infrared, millimeter, and radio wavelengths, where the extinction is much smaller.

To investigate the birth process and early evolution of massive stars, we are carrying out a multiwavelength study of a sample of 18 luminous *IRAS* sources in the southern hemisphere thought to be representative of young massive star-forming regions. The goal is to understand the physical and chemical differences between different stages of evolution. The objects were taken from the Galaxy-wide survey of CS(2→1) emission (Bronfman et al. 1996) toward *IRAS* sources with far-infrared colors typical of compact H II regions (Wood & Churchwell 1989). We selected sources based primarily on the observed CS(2→1) line profiles; looking for self-absorbed profiles consistent with inward or outward motions (e.g., Mardones 1998), and/or with extended line wings, possibly indicating the presence of bipolar outflows. In addition, the sources were required to have *IRAS* 100 μm fluxes greater than 10^3 Jy and to have declination $\delta < -20^\circ$. The luminosity of the *IRAS* sources, computed using the *IRAS* fluxes and distances derived by L. Bronfman (2006, private communication) are in the range $1 \times 10^4 - 4 \times 10^5 L_{\odot}$, implying that they contain at least one embedded massive star. The characteristics of the radio continuum emission at 1.4–8.6 GHz of the ionized gas and of the cold dust emission at 1.2 mm associated with the *IRAS* sources in our sample are reported, respec-

Electronic address: emorales@mpifr-bonn.mpg.de

¹ Current address: Max-Planck-Institut für Radioastronomie, Auf dem Hügel 69, 53121 Bonn, Germany.

² For part of this work affiliated with Departamento de Astronomía, Universidad de Chile, Casilla 36-D, Santiago, Chile

tively, in the first and second papers of the series (Garay et al. 2006, 2007, hereafter Paper I and Paper II, respectively).

Here, we report the results of mid-infrared (MIR) N -band and Q -band imaging observations, and N -band spectroscopy toward a selection of sources in our original sample. The MIR continuum emission was imaged within regions of typically $\simeq 30'' \times 30''$ centered on the *IRAS* sources, with an angular resolution of $\simeq 1''$. In addition, *Spitzer* images at 3.6, 4.5, 5.8, 8.0, and 24 μm were obtained from the public data of the galactic surveys Galactic Legacy Infrared Mid-Plane Survey Extraordinaire (GLIMPSE) and MIPS Galactic Plane Survey (MIPSGAL). The primary goals of this study are to compare the MIR observations with the radio continuum images of similar angular resolution (Paper I), to determine the characteristics and physical conditions of the warm dust surrounding recently formed massive stars, and to investigate the stellar content within the massive and dense cores.

In Section 2, we describe the MIR observations and data reduction. Section 3 presents the images and spectra, the overall results and computed parameters of the sample. In Section 4, we present further discussion, and in Section 5 the conclusions of this study.

2. OBSERVATIONS AND DATA REDUCTION

The N - and Q -band images and N -band spectra were obtained using the TIMMI2 mid-infrared camera (Reimann et al. 2000) mounted on the ESO 3.6 m telescope at La Silla, Chile. The camera uses a Raytheon 320×240 Si:As impurity band conduction high background array. A pixel scale of $0.3''$ was used for N -band imaging observations and $0.2''$ for Q -band images. We performed long-slit low-resolution spectroscopy ($70''$ north-south oriented slit, $\Delta\lambda/\lambda \sim 160$) using a pixel scale of $0.45''$ and a slit width of $1.2''$ or $3.0''$.

The observations were carried out during 2003 May 23–25. The TIMMI2 filters used were N1 ($\lambda_{\text{eff}} = 8.7 \mu\text{m}$, $\Delta\lambda = 1.2 \mu\text{m}$), N11.9 ($\lambda_{\text{eff}} = 11.7 \mu\text{m}$, $\Delta\lambda = 1.2 \mu\text{m}$), and Q1 ($\lambda_{\text{eff}} = 17.7 \mu\text{m}$, $\Delta\lambda = 0.8 \mu\text{m}$). We imaged 14 sources in at least one filter in the N -band region; and nine of them in the Q -band region. N -band spectroscopy ($8-13 \mu\text{m}$) was made toward eight sources. The standard nodding/chopping observing technique was used to remove the strong and variable thermal background emission. For imaging, most sources were observed in the *small-source* mode (chopping in the north-south direction, nodding in the east-west direction) using large throws ($\gtrsim 30''$), in order to detect the extended MIR emission. For spectroscopy, in general, smaller chop throws were selected ($\simeq 20''$). MIR calibration standards stars — HD 108903, HD 123139 and HD 169916 —, were observed in different modes (imaging and spectroscopic) every couple of hours for photometric flux conversion and spectroscopic calibration. Table 1 summarizes all the observations: Columns 1 and 2 indicate the *IRAS* source identification and galactic coordinates, respectively; Column 3 gives the TIMMI2 filter (designated by its effective wavelength λ_{eff} or by the range $8-13 \mu\text{m}$ for the case of spectroscopy); Column 4 indicates the final on-source integration time; Column 5 indicates the field of view (FOV; east-west amplitude \times north-south amplitude for images, slit width \times north-south amplitude for spectra); and finally Column 6 lists the noise level after calibration (images: noise level in 1 arcsec², spectra: average error in the full FOV integrated spectrum).

The images were reduced using our own IDL routines based on scripts originally developed by M. Marengo (2004, private

TABLE 1
SUMMARY OF THE TIMMI2 OBSERVATIONS

IRAS source	Galactic name	Filter ^a (μm)	Time (s)	FOV ^b ($[''] \times [']$)	Noise ^c (mJy)
12383–6128	G301.731+1.104	8.7	662	30×25	8
		11.7	994	40×30	5
		17.7	662	20×20	70
13291–6249	G307.560–0.586	8–13	767	3.0×20	185
		8.7	662	40×30	8
		17.7	1027	20×15	35
14095–6102	G312.596+0.048	8–13	640	1.2×15	187
		14593–5852	G319.163–0.419	8.7	729
15502–5302	G328.307+0.432	17.7	662	20×20	46
		15520–5234	G328.808+0.632	11.7	371
16128–5109	G332.153–0.445	11.7	795	40×30	5
		8–13	580	30×20	41
		8–13	640	1.2×20	119
16458–4512	G340.248–0.373	8.7	66	96×35	16
		11.7	431	30×25	7
		8–13	320	1.2×20	432
16524–4300	G342.704+0.130	11.7	795	30×15	6
		17.7	646	64×15	42
		8–13	640	1.2×20	134
17008–4040	G345.499+0.354	11.7	1325	30×15	4
		11.7	298	30×15	9
17009–4042	G345.490+0.311	17.7	464	20×25	66
		8–13	640	1.2×20	603
		11.7	662	30×15	6
17016–4124	G345.001–0.220	17.7	662	64×15	44
		8–13	639	3.0×20	410
		11.7	1275	40×30	4
17158–3901	G348.534–0.973	17.7	397	20×15	50
		8–13	639	3.0×20	81
		11.7	1076	30×30	4
17271–3439	G353.416–0.367	17.7	497	64×15	71
		11.7	1656	40×30	3

^a 8.7, 11.7 and 17.7 μm refer to N1, N11.9 and Q1 images, respectively, whereas the 8–13 μm range corresponds to long-slit low-resolution spectroscopy.

^b FOV estimated depending on the observing mode. For the *small-source* imaging mode (nodding in the east-west direction, chopping in the north-south direction): FOV = nod throw \times chop throw. For the *classic* imaging mode (both nodding and chopping in the north-south direction): FOV = array x -size ($96''$ for N and $64''$ for Q) \times nod throw. For spectra: FOV = slit width \times nod throw.

^c For images, the value listed is the noise level in 1 arcsec² after flux calibration; for spectra, we give the average error in the spectrum that includes the whole emission.

communication). Basically, the chopping and nodding pairs corresponding to a single chop-nod cycle were co-added in an individual frame, and then each useful portion in that image was bari-centered before the combination of all the frames. This prevented us from losing angular resolution due to little offsets between different chop-nod cycles. The final image for each source was produced co-adding all the observations weighted by the integration times. The flux calibration was made using the tabulated fluxes for the standard stars given on the instrument Web page (based on preliminary versions of the spectral models by Cohen et al. 1999). Finally, the images were Gaussian smoothed to a resolution of $\simeq 1.8''$, in order to enhance the sensitivity to diffuse extended emission and to match the angular resolution of the *Spitzer*–GLIMPSE images (see below), allowing us to compare both sets of data in a consistent way.

For spectra reduction we used the IDL scripts provided by Siebenmorgen et al. (2004), slightly modified in order to include the extended emission in the spectra extraction. This method is based on the optimal extraction described by Horne (1986), and consists of summing along the spatial dimension after weighting by a source profile, which is computed by collapsing the image along the dispersion direction. Wave-

TABLE 2
OBSERVED PARAMETERS

Source	α (J2000)	δ (J2000)	θ^a ($''$)	$F_{8.7\mu\text{m}}^{\text{point}}$ (mJy)	$F_{11.7\mu\text{m}}^{\text{point}}$ (mJy)	$F_{17.7\mu\text{m}}^{\text{point}}$ (mJy)	$F_{8.7\mu\text{m}}^{\text{tot}}$ (mJy)	$F_{11.7\mu\text{m}}^{\text{tot}}$ (mJy)	$F_{17.7\mu\text{m}}^{\text{tot}}$ (mJy)
12383–6128	12 41 17.66	–61 44 41.0	2.2	975 ± 97	1480 ± 140	11300 ± 2580	5520 ± 566	6370 ± 611	31800 ± 7670
13291–6249	13 32 31.18	–63 05 18.5	0.7	3860 ± 369	...	19100 ± 5180	9010 ± 871	...	63000 ± 17100
14095–6102	14 13 14.22	–61 16 48.8	3520 ± 400	...
14593–5852 I	15 03 13.64	–59 04 29.9	3.3	1510 ± 149	...	17700 ± 4880	4530 ± 458	...	45100 ± 12400
14593–5852 II	15 03 12.60	–59 04 31.5	3.0 ^b	< 81 ^c	...	9150 ± 2520	< 285 ^c	...	20700 ± 5740
15502–5302 I	15 54 06.33	–53 11 40.1	2.0	...	45300 ± 4240	73600 ± 6890	...
15502–5302 II	15 54 05.20	–53 11 40.4	2.3	...	2870 ± 270	4510 ± 425	...
15520–5234	15 55 48.28	–52 43 06.7	1.1	...	4780 ± 505	19300 ± 6610	...	11400 ± 1210	73000 ± 25000
16128–5109	16 16 40.22	–51 17 11.8	...	2240 ± 242	6210 ± 661	...	29400 ± 3680	101000 ± 10700	...
16458–4512	16 49 30.02	–45 17 44.4	1.2	...	3010 ± 294	13100 ± 3180	...	5860 ± 577	28400 ± 6960
16524–4300	16 56 03.47	–43 04 41.6	348 ± 40	1990 ± 234	...
16547–4247	16 58 16.55	–42 52 04.2	280 ± 28 ^d	...
17008–4040 I	17 04 22.82	–40 44 22.6	0.9	...	15000 ± 1630	62800 ± 14200	...	18300 ± 1990	80200 ± 18100
17008–4040 II	17 04 23.48	–40 44 35.7	1.4	...	861 ± 100	5240 ± 1210	...	1010 ± 119	5360 ± 1280
17009–4042	17 04 28.02	–40 46 24.8	1.6	...	9570 ± 1060	45700 ± 10400	...	22600 ± 2510	141000 ± 32200
17016–4124 I	17 05 11.18	–41 29 06.6	1.1	...	951 ± 102	7620 ± 2370	...	1580 ± 174	14900 ± 4660
17016–4124 II	17 05 10.98	–41 29 14.1	1.1	...	857 ± 92	7100 ± 2210	...	1060 ± 116	7880 ± 2490
17158–3901	17 19 15.47	–39 04 32.5	1.2	...	1460 ± 155	6240 ± 1880	...	8780 ± 936	25400 ± 7770
17271–3439	17 30 28.55	–34 41 48.8	0.7	...	838 ± 89	10900 ± 1170	...

NOTE. — Units of right ascension are hours, minutes, and seconds, and units of declination are degrees, arcminutes, and arcseconds. The position is from the brightest component when the source is multiple; astrometry was performed using the *Spitzer*–IRAC images. F^{point} is the flux density calculated on compact sources using $2.0''$ radius aperture photometry. F^{tot} is the flux density calculated on a region enclosing the total emission from each source. 1σ errors are given, taking into account statistical and calibration uncertainties.

^a The angular size θ is the deconvolved FWHM, computed as $\theta = \sqrt{\text{FWHM}^2 - \text{FWHM}_{\text{std}}^2}$, where FWHM is determined on the N -band image ($11.7\mu\text{m}$ when available, $8.7\mu\text{m}$ otherwise) for the compact source, and FWHM_{std} is the averaged value of the standard stars in the corresponding filter.

^b Angular size computed at $17.7\mu\text{m}$.

^c 3σ upper limit.

^d From Brooks et al. (2003), assuming a flux uncertainty of 10%.

length calibration was done mainly using the tables given in the Web page. The same procedure was applied to the target and the corresponding standard star, whose theoretical spectrum (models by Cohen et al. 1999) was used to calibrate the final target spectrum.

We complemented our observations with MIR data obtained by the *Spitzer Space Telescope* (Werner et al. 2004). Images at 3.6 , 4.5 , 5.8 , and $8.0\mu\text{m}$ were downloaded from the public data of the GLIMPSE Legacy Program (Benjamin et al. 2003), that surveyed the plane in the four bands of the Infrared Array Camera (IRAC; Fazio et al. 2004). We also obtained images at $24\mu\text{m}$ from the recently delivered mosaics of the MIPS GAL Legacy Program (Carey et al. 2009), carried out using the Multiband Imaging Photometer for *Spitzer* (MIPS; Rieke et al. 2004). The 18 sources of our multiwavelength survey are within the (l, b) range covered by GLIMPSE/GLIMPSE II and MIPS GAL, except IRAS 12383–6128 which has only data at 4.5 and $8.0\mu\text{m}$. The angular resolutions of the used *Spitzer* filters, calculated from the point-spread function (PSF) archives given in the telescope Web page, are $1.81''$, $1.76''$, $1.84''$, $2.14''$, and $5.81''$ at 3.6 , 4.5 , 5.8 , 8.0 , and $24\mu\text{m}$, respectively.

3. RESULTS

3.1. TIMMI2 Images

We detected MIR emission toward the observed regions in all the observed filters. Figures 1 and 2 show gray-scale images of the smoothed emission in the N -band ($8.7\mu\text{m}$ or $11.7\mu\text{m}$) toward 12 regions. We do not show images of the emission toward IRAS 14095–6102 and 16524–4300, which have a low signal-to-noise ratio (S/N). In seven regions, we detected a single MIR source. Most of these have a cometary-like morphology, exhibiting a bright compact component at

the head and a weak trailing extended emission. In three regions (IRAS 15502–5302, 17016–4124, and 17008–4040) we detected the presence of two distinct MIR objects, and in two regions (IRAS 16128–5109 and 17271–3439) the MIR emission has a complex morphology. The morphologies of the sources detected in both the N and Q bands are very similar. The only exception is in the IRAS 14593–5852 region, where we detected a source at $17.7\mu\text{m}$ (14593–5852 II) which is not seen in the N filter (see Figure 3).

Among the compact components, no one is strictly point-like: whereas the average FWHM size of the standard stars is $0.9''$ in the $8.7\mu\text{m}$ filter, $1.2''$ at $11.7\mu\text{m}$, and $1.3''$ at $17.7\mu\text{m}$, the compact components have FWHM sizes $\gtrsim 1.4''$ and $\gtrsim 1.5''$ at $11.7\mu\text{m}$ and $17.7\mu\text{m}$, respectively. However, we do not discard the presence of point sources in a few cases, due to the uncertainties in the FWHM determination, which was made using a radial profile fitting.

According to Saviane & Doublier (2005), the pointing accuracy of the ESO 3.6 m telescope is $\simeq 5''$ which prevents a direct comparison of the MIR and radio continuum spatial distributions. We used the *Spitzer*–IRAC data to determine accurate astrometry of our images. The bright compact part of the smoothed TIMMI2 image was fitted to the corresponding peak in the longest wavelength IRAC image available (usually the $8.0\mu\text{m}$ image). In most cases, the morphology of the emission exhibited in the IRAC and our images are very similar, allowing us to match the positions without any confusion. The offsets between the original TIMMI2 coordinates and the new adjusted positions are typically $\simeq 11''$. Since the GLIMPSE point-source accuracy is $\simeq 0.3''$ (Meade et al. 2005), we estimate that our final TIMMI2 coordinates have an error $\lesssim 1''$, produced by centering uncertainties (e.g., corresponding regions not compact enough or peaks not well de-

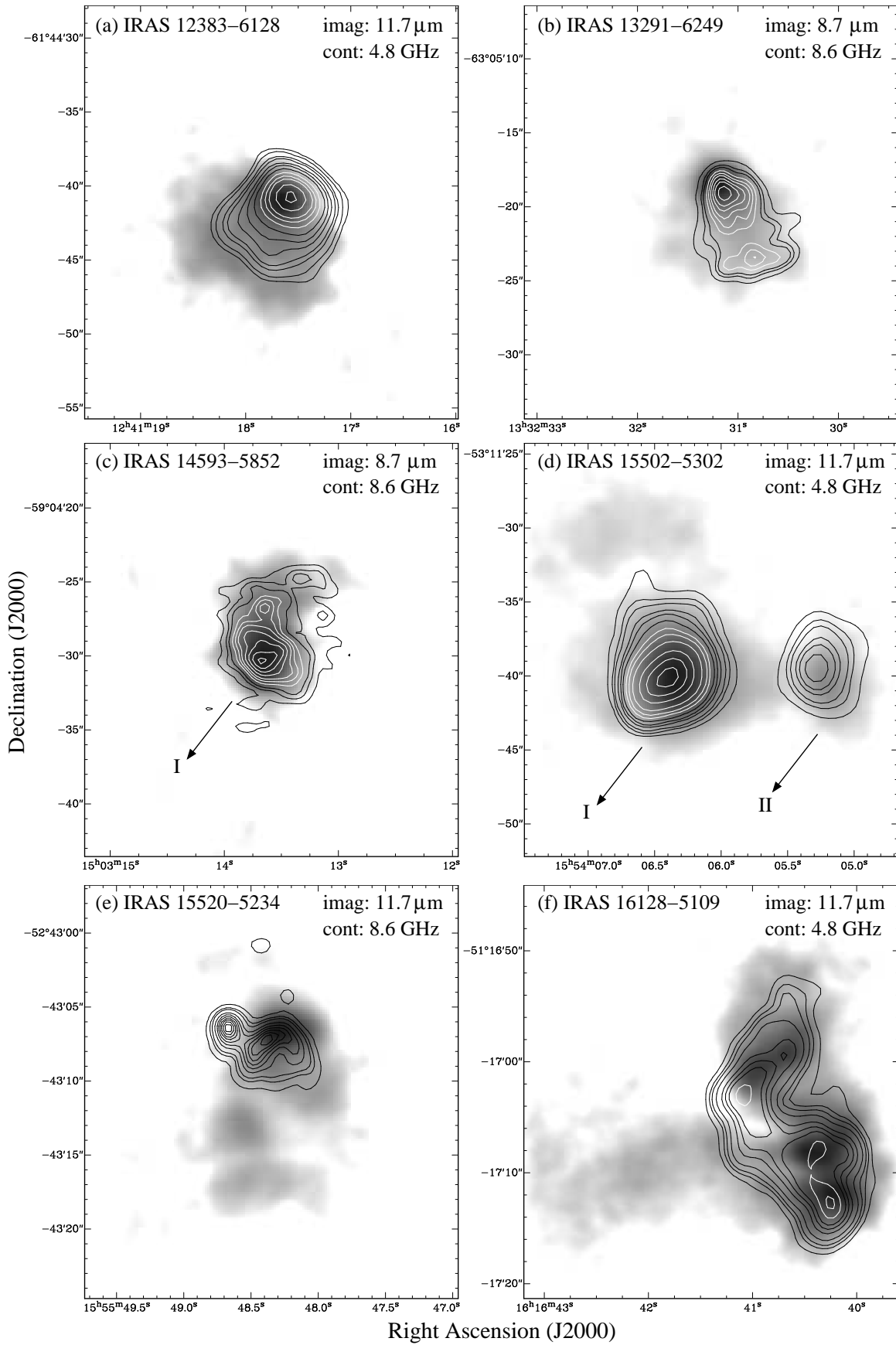


FIG. 1.— TIMMI2 *N*-band gray-scale images, overlaid with radio continuum ATCA contours. Source names are shown in the upper left corner, whereas the upper right corner indicates the specific TIMMI2 filter used (11.7 or 8.7 μm) and the frequency of the radio contours (4.8 or 8.6 GHz). The images are displayed in logarithmic scale, over the full flux range. Contour levels are basically the same than those used in Paper I.

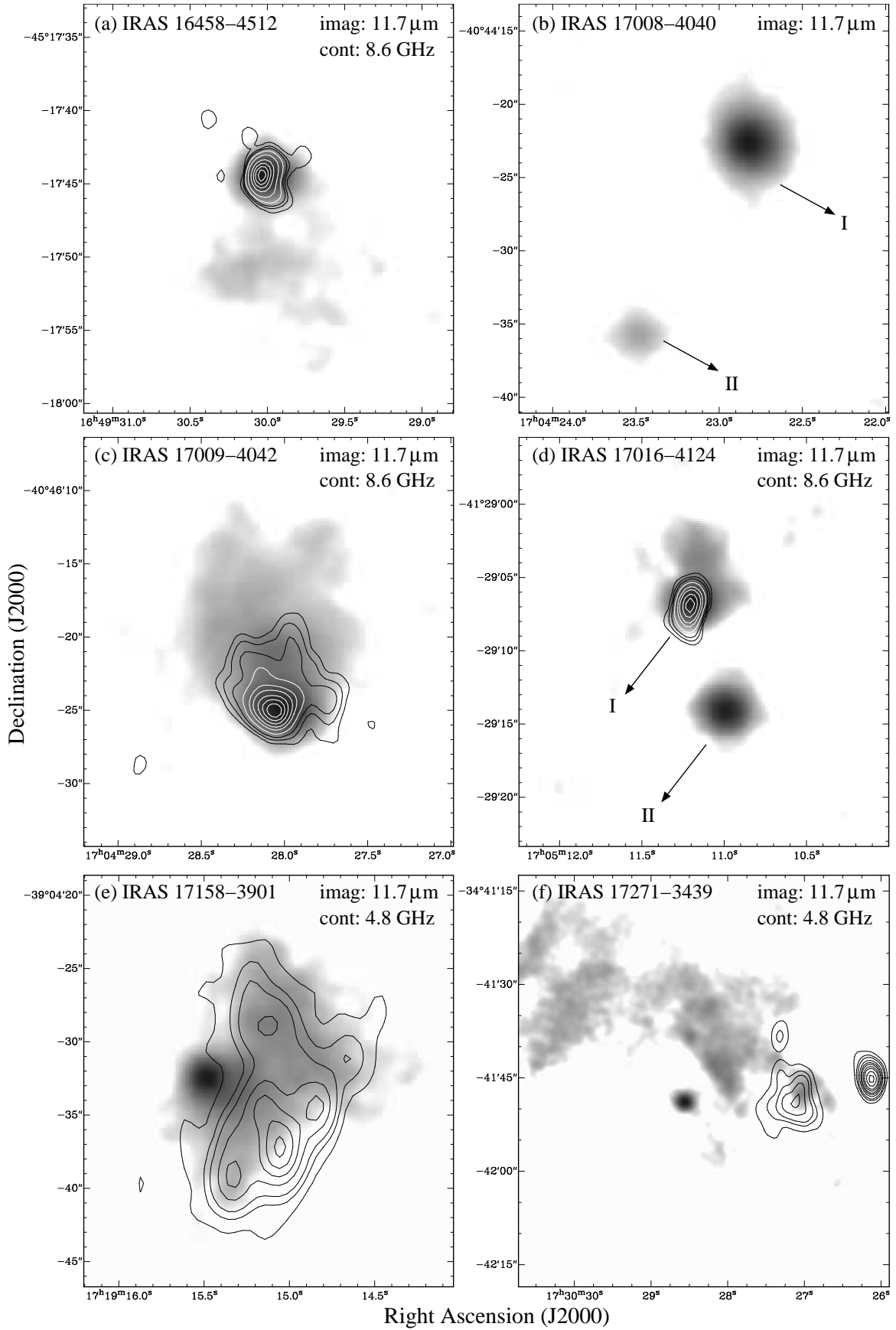


FIG. 2.— Same as in Figure 1. (b) For IRAS 17008–4040, no radio continuum emission was detected toward objects I and II up to a level of 1.5 mJy at 4.8 GHz.

fined).

Figures 1 and 2 also show contour maps of the radio continuum emission (Paper I, 4.8 or 8.6 GHz) overlaid on the N -band images. These figures show that in most sources the spatial distribution of the radio and MIR emissions are highly correlated, both in extended (IRAS 12383–6128, 13291–6249, 14593–5852, 15502–5302, 16128–5109, and 17009–4042) and compact structures (the same sources, together with IRAS 15520–5234, 16458–4512, and 17016–4124 I). This suggests an intimate association between the ionized gas and the warm dust within these regions (see further discussion in Section 4.2). Although in five (of 10) compact sources the corresponding radio and MIR peaks are slightly shifted, the displacement never reaches more than $\simeq 1''$ and therefore does not affect the global morphological match. Since these shifts are small, they probably can be explained uniquely by positional uncertainties of the data. The exceptional cases in which an MIR source is not associated with radio continuum emission will be discussed in Section 4.4.

Table 2 lists the source properties computed directly from the TIMMI2 images (positions, angular sizes, and flux densities). For each source, the given position corresponds to the centroid of the compact component; the brightest compact object is taken as a reference when the region is complex. The angular size was calculated as $\theta = \sqrt{\text{FWHM}^2 - \text{FWHM}_{\text{std}}^2}$, where FWHM is the full width half-maximum of the compact component and FWHM_{std} is the averaged value of the observed standard stars, both calculated by fitting the radial profile on the N -band image ($11.7 \mu\text{m}$ when available, $8.7 \mu\text{m}$ otherwise). We computed two flux densities: a “point-source” flux density F^{point} , calculated on compact sources using a $2.0''$ radius aperture photometry (diameter of about twice the smoothed resolution of $1.8''$), and a “total” flux density F^{tot} , calculated on a region (circular in almost all cases) enclosing the whole emission from each source. Photometric error was computed adding by quadrature the statistical noise of the image and the flux calibration error, which is mainly determined by the atmospheric fluctuations. We estimated this contribution as the standard deviation of the calibration factor along the three nights of observation. The resulting total photometric error is $\simeq 10\%$ for the 8.7 and $11.7 \mu\text{m}$ filters and $22\% - 34\%$ for the $17.7 \mu\text{m}$ filter, which is affected by the presence of many atmospheric features within the filter wavelength range.

Within the 14 regions observed with TIMMI2, we can identify at least 15 simple bright compact sources with N -band deconvolved FWHM sizes in the range $0.7'' - 3.3''$ (θ in Table 2). Using the kinematical distances, the physical diameters of these objects are in the range $0.008 - 0.18$ pc, with an average value of 0.03 pc. The physical sizes of the compact MIR components associated with radio continuum sources are in good agreement with each other, when measured at a comparable angular resolution (at 8.6 GHz). This supports the idea that the radio and MIR emission trace similar structures.

3.2. Spitzer Images

Spitzer and Q -band images of all sources are shown in a dedicated Web page³. In this Web page we further discuss the characteristics of the MIR emission toward each of the individual regions of the survey and summarize what is already known about them in the literature. In general, the IRAC images show similar structures to those seen in the TIMMI2 images, although the former are much more sensitive to diffuse

TABLE 3
Spitzer FLUXES

Source	$F_{3.6\mu\text{m}}^{\text{tot}}$ (mJy)	$F_{4.5\mu\text{m}}^{\text{tot}}$ (mJy)	$F_{5.8\mu\text{m}}^{\text{tot}}$ (mJy)	$F_{8.0\mu\text{m}}^{\text{tot}}$ (mJy)	$F_{24\mu\text{m}}$ (mJy)
12383–6128	... ^a	460	... ^a	7980	... ^a
13291–6249	1140	> 1990 ^b	6290	> 8370 ^b	> 32400 ^c
14095–6102	158	219	1770	4410	69300 ^d
14593–5852 I	255	411	1670	4660	> 32100 ^{ce}
14593–5852 II	< 33 ^f	< 44 ^f	< 347 ^f	< 950 ^f	...
15394–5358	878	5050 ^d	> 7710 ^b	9840 ^d	46900 ^d
15502–5302 I	1160	> 2380 ^b	11000	> 13300 ^b	> 27800 ^{ce}
15502–5302 II	111	174	802	2090	...
15520–5234	315	936	2760	6560	55600 ^d
15596–5301	128	352	1040	1870	44900 ^d
16128–5109	2860	3950	17700	53300	> 12300 ^c
16272–4837	87	317	432	389	6040
16458–4512	188	423	1890	4530	76000 ^d
16524–4300	366	955	2940	5410	65800 ^d
16547–4247	119	564	988	913	49900 ^d
17008–4040 I	557	9640 ^d	23700 ^d	45100 ^d	> 49500 ^{ee}
17008–4040 II	27	53	359	883	...
17009–4042	470	1560	5920	> 12800 ^b	> 63800 ^c
17016–4124 I	71	442	1010	2040	195000 ^{de}
17016–4124 II	25	48	242	677	...
17158–3901	488	528	3000	8350	> 54300 ^c
17271–3439	1020	1430	8440	24600	> 5130 ^c

NOTE. — F^{tot} is the flux density calculated on the same region as for TIMMI2 photometry. Uncertainties are estimated to be $\simeq 20\%$ for the non-saturated IRAC bands.

^a Out of GLIMPSE/MIPSGAL coverage.

^b Saturated; lower limit obtained integrating the emission in the TIMMI2-defined region.

^c Saturated; lower limit obtained using $35''$ radius aperture photometry.

^d Saturated; recovered flux using the *imageworks* PSF fitting tool (see the text).

^e Double sources not resolved. Flux includes components I and II.

^f Upper limit obtained integrating the diffuse emission in the TIMMI2-defined region.

extended emission, at 5.8 and $8.0 \mu\text{m}$. To illustrate this, we show in Figures 3 and 4 two examples of three-color images made combining the individual 3.6, 4.5, and $8.0 \mu\text{m}$ IRAC bands, together with the corresponding N and Q -band images from TIMMI2. These two regions are those containing the most promising high-mass protostellar object (HMPO) candidates (see Section 4.4). The diffuse emission seen in the 5.8 and $8.0 \mu\text{m}$ IRAC filters, not detected with TIMMI2, is not associated with radio continuum emission from ionized gas and probably contains a considerable contribution from polycyclic aromatic hydrocarbon (PAH) emission bands at 6.2, 7.7, and $8.6 \mu\text{m}$ (see Section 4.3). In addition, due to its higher sensitivity and shorter wavelengths available, the IRAC images reveal that in most cases the TIMMI2 source is the brightest one of a cluster of MIR objects.

Some of the three-color images show the presence of IR features that appear greenish (the so-called green fuzzies), most of which are extended and not associated with radio continuum emission. This type of emission is found toward IRAS 15394–5358, 15520–5234, 15596–5301, 16272–4837, 16547–4247, 17008–4040 (Figure 4), and 17016–4124. Beuther et al. (2005) and Rathborne et al. (2005) first suggested that the bright and extended IRAC $4.5 \mu\text{m}$ emission might trace shocked gas by outflowing material ramming in the ambient interstellar medium. Indeed, numerical simulations predict that the contribution of H_2 shock-excited line emission in the $4.5 \mu\text{m}$ band is an order of magnitude brighter

³ http://www.mpifr-bonn.mpg.de/staff/emorales/mir_individual/mir_individual.html

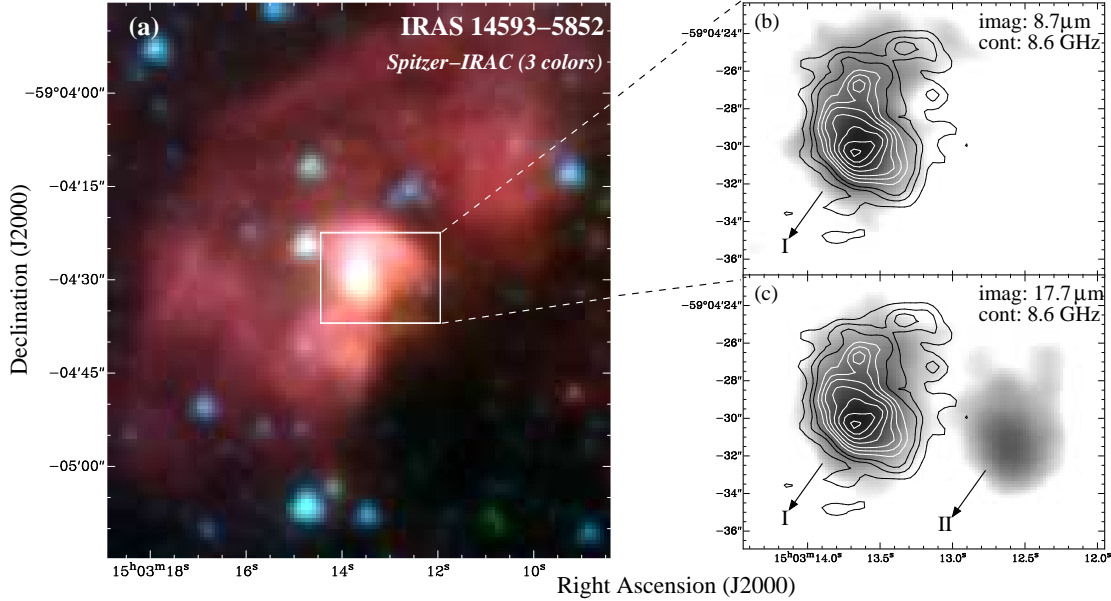


FIG. 3.— IRAS 14593–5852. (a) *Spitzer*–IRAC image made using 3.6 (blue), 4.5 (green), and 8.0 μm (red) bands. (b) TIMMI2 8.7 μm gray-scale image, overlaid with ATCA 8.6 GHz contours. (c) TIMMI2 17.7 μm gray-scale image, overlaid with ATCA 8.6 GHz contours.

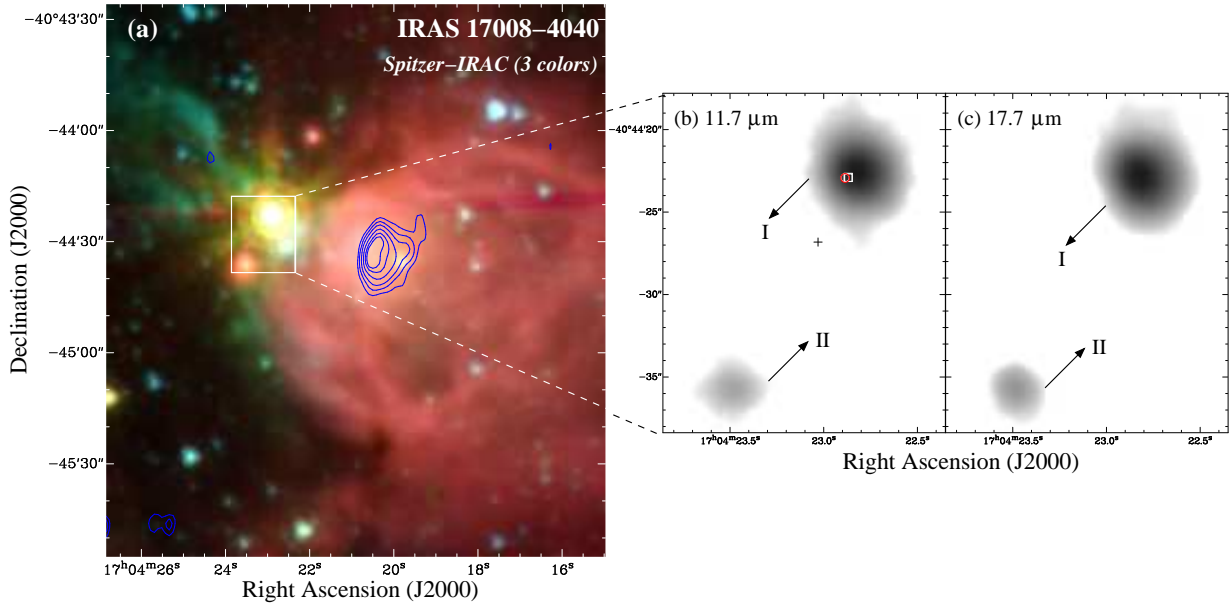


FIG. 4.— IRAS 17008–4040. (a) *Spitzer*–IRAC image made using 3.6 (blue), 4.5 (green), and 8.0 μm (red) bands. Also shown are ATCA contours (in blue) at 2.5 GHz. (b) TIMMI2 11.7 μm gray-scale image, with the locations of maser sites indicated by small symbols: OH main-line by a white square (Caswell 1998), 6.7-GHz methanol by a red circle (Walsh et al. 1998), and water vapor by a black cross (Forster & Caswell 1989). (c) TIMMI2 17.7 μm gray-scale image.

than in the other IRAC bands (Smith & Rosen 2005). Observational support for this interpretation has been provided by recent *Spitzer* surveys (e.g., Noriega-Crespo et al. 2004; Smith et al. 2006), which show that molecular outflows are particularly strong in the 4.5 μm band. We also found that most of the sources which exhibit green fuzzies (all but IRAS 15596–5301 and 17008–4040) are embedded in large-scale 8.0 μm extinction features known as infrared dark clouds (IRDCs), which host the earliest stages of high-mass star formation (see Rathborne et al. 2005, and references therein).

All the sources of our multiwavelength survey covered by MIPS GAL present very bright emission at 24 μm , quite saturated at the core of the PSF (with the exception of IRAS 16272–4837); in particular, the TIMMI2 objects lie

just within these saturated cores. In some regions, interesting large-scale structures could be seen at 24 μm , hinting the presence of warm dust probably excited by our target sources beyond the FOV studied with TIMMI2. We tried to overcome the saturation and rescue the lost MIPS fluxes using the publicly available *imageworks* code⁴ written by T. Jarrett, which recovers the saturated pixels by applying a PSF model that is fit to the nonsaturated wings of the source. However, since most of our sources are embedded, the PSF wings are often contaminated by diffuse emission and the recovered flux was overestimated by the code. We therefore only consider valid those fluxes which are consistent with our spectral energy dis-

⁴ <http://spider.ipac.caltech.edu/staff/jarrett/irac/index-1.html>

tribution (SED) models, as described in Section 4.1; they are listed in the last column of Table 3. For the remaining sources, we give lower limit fluxes, obtained by integrating the emission of the PSF wings within an aperture of $35''$ and applying the aperture correction of Engelbracht et al. (2007).

Table 3 gives also the results of the photometry obtained from the IRAC images. In order to compare properly with TIMMI2 data, we integrated the emission across the same regions as for the TIMMI2 photometry, even though the emission in the IRAC images is usually more extended. This resulted, however, in a good correlation between *MSX* $8.3 \mu\text{m}$ and IRAC $8.0 \mu\text{m}$ fluxes (see Section 4.1), indicating that the regions selected for photometry were appropriate. For the sources not observed with TIMMI2, we chose similar apertures ($\simeq 6''$ – $9''$ radius) enclosing the brightest source(s). According to Meade et al. (2005), magnitude uncertainties are estimated to be less than 0.2 for the GLIMPSE Catalog, corresponding to a flux error of $\lesssim 18\%$. Considering that our sources are not pointlike, we estimated our photometric uncertainty as 20%. For the saturated sources, we proceeded as for MIPS photometry, applying the *imageworks* code and considering the recovered flux only if it is consistent with the SED model; otherwise, we give a lower limit flux integrated within the TIMMI2-defined region.

3.3. TIMMI2 Spectra

Figure 5 presents the 8 – $13 \mu\text{m}$ spectra of the eight observed sources, extracted within small angular apertures of $\simeq 4''$ – $8''$ around the central positions of the spectral images. The north-south oriented slit was centered in the brightest part of each source. The spectra integrated in the whole emission regions, not shown here, exhibit practically the same shape and features, but logically with a different flux scale. We truncated the spectra at $8.2 \mu\text{m}$ due to calibration uncertainties at the lower wavelength edge. Error bars are plotted as filled regions around the main curve; they only represent the statistical noise derived from the original spectral image and do not include other causes of error.

All the spectra exhibit a broad — and in most cases prominent — silicate band seen in absorption, at $\simeq 9.7 \mu\text{m}$. Seven sources (all but IRAS 17008–4040 I, Figure 5(f)) present [Ne II] line emission at $\simeq 12.8 \mu\text{m}$, which is spatially extended. This is consistent with the association of these sources with radio continuum emission of ionized gas. Column 2 of Table 4 gives the [Ne II] line flux measured on the integrated spectrum of each source; the statistical uncertainties derived directly from the spectrum are $\lesssim 2\%$. Emission in other two atomic fine-structure lines, [Ar III] at $9.0 \mu\text{m}$ and [S IV] at $10.5 \mu\text{m}$, was observed toward IRAS 16128–5109 (Figure 5(d)), but this is more evident in the integrated spectrum). The [Ar III] is also present in IRAS 13291–6249 (Figure 5(b)). The PAH features at $11.3 \mu\text{m}$ and $8.6 \mu\text{m}$ were detected in only one region (IRAS 12383–6128, Figure 5(a)). The faint emission feature at $\simeq 9.7 \mu\text{m}$ in IRAS 13291–6249, 15520–5234, and 17016–4124 I (Figures 5(a), (c), and (h), respectively) could correspond to the H_2 0–0 $S(3)$ line, but it is located in a wavelength range highly contaminated by telluric ozone features, which make noisier this part of the spectrum (note that this is in general not properly represented by the statistical noise shown in the spectra). We therefore label this line with a question mark in Figure 5. If present, the H_2 0–0 $S(3)$ line could be tracing a photodissociation region or the existence of shock events, since it can be either radiatively or collisionally excited (see, e.g., Morris et al. 2004).

TABLE 4
PARAMETERS DERIVED FROM TIMMI2 SPECTRA

Source	Flux [Ne II] ^a ($10^{-15} \text{ W m}^{-2}$)	T_d ^b (K)	$N(\text{H}_2)_{\text{cold}}$ ^b (10^{22} cm^{-2})	$N(\text{H}_2)_{1.2 \text{ mm}}$ ^c (10^{22} cm^{-2})
12383–6128	9.7	369	8.9	5.6
13291–6249	16.4	759	11.6	9.0
15520–5234	7.1	355	13.6	24.8
16128–5109	83.2	233	6.6	9.1
16458–4512	10.1	405	13.8	10.2
17008–4040 I	13.9	339	17.1	21.4
17009–4042	31.1	458	13.8	32.2
17016–4124 I	2.5	... ^d	... ^d	31.3

^a Uncertainties derived from the spectra are $\lesssim 2\%$ (only statistical error).

^b Best fit parameters; see Equation (1). Uncertainties are $< 1\%$, but we consider them underestimated (see the text).

^c Computed from Equation (5). Uncertainties are $\simeq 20\%$, only considering the error from the 1.2 mm flux.

^d Low-quality spectrum.

We fitted the continuum part of the TIMMI2 spectrum (i.e., removing first the line features) using a simple model (Pascucci et al. 2004) which assumes that the MIR continuum flux arises from a small region of hot dust, whose emission can be described by a gray body with temperature T_d , column density $N(\text{H}_2)_{\text{hot}}$, and solid angle Ω_d , surrounded by a larger cloud of cold dust with column density $N(\text{H}_2)_{\text{cold}}$. Under these assumptions, the flux density as a function of frequency is given by

$$F_\nu = \Omega_d B_\nu(T_d) (1 - e^{-\sigma_\nu N(\text{H}_2)_{\text{hot}}}) e^{-\sigma_\nu N(\text{H}_2)_{\text{cold}}/2} , \quad (1)$$

where

$$\sigma_\nu = R_{\text{dg}} \mu m_{\text{H}} \kappa_\nu . \quad (2)$$

R_{dg} is the dust-to-gas mass ratio, μ is the mean molecular weight per hydrogen molecule, m_{H} is the hydrogen mass, and κ_ν is the absorption opacity per mass of dust, whose tabulated values were taken from the Weingartner & Draine (2001) dust model, with $R_V = 5.5$. Chapman et al. (2009) found that this model is more consistent with the MIR extinction law of high-density regions than the Weingartner & Draine (2001) model with $R_V = 3.1$, because it includes larger dust grains and therefore accounts for possible grain growth. The fitting procedure uses equation (1) with Ω_d , T_d , and $N(\text{H}_2)_{\text{cold}}$ as free parameters. We constrain the parameter $N(\text{H}_2)_{\text{hot}}$ by imposing the condition that

$$N(\text{H}_2)_{\text{hot}} = \sqrt{\frac{\Omega_d}{\Omega_c}} N(\text{H}_2)_{\text{cold}} , \quad (3)$$

where Ω_c is the solid angle subtended by the cold component. This condition, which arises by assuming constant density and spherical symmetry for both the hot and cold components, is imposed in order to overcome the degeneracy problem of the parameters $N(\text{H}_2)_{\text{hot}}$ and Ω_d , as was done for the SEDs fitting (see Section 4.1). We use as angular size of the cold cloud that determined from the 1.2 mm emission (Paper II).

Columns 3 and 4 of Table 4 list the parameters T_d and $N(\text{H}_2)_{\text{cold}}$ obtained from the best fit to the spectrum extracted from the central part of each source. The best fit for each source is shown in Figure 5 as a dashed line. We assumed $R_{\text{dg}} = 1/125$ (Draine 2003) and $\mu = 2.8$ (mean molecular weight, adopting 10% abundance of He with respect to H). The uncertainties derived from the covariance matrix computed in the least-square minimization are $< 1\%$, but we sus-

pect that they are significantly underestimated, since the fitting only considers the statistical noise in the spectra, which is also low.

To assess the robustness of the derived values of the parameters we investigated the effects produced by changes in the assumptions. First, we used the Weingartner & Draine model for the opacities with $R_V = 3.1$. Since for the TIMMI2 spectral range, the $R_V = 5.5$ and $R_V = 3.1$ models do not present significant differences, we found that the fitting procedure is not sensitive to such change, and the adjusted parameters only differ by $\simeq 5\%$ in T_d and $\simeq 3\%$ in $N(\text{H}_2)_{\text{cold}}$.

The average optical depths between 8 and 13 μm inferred from the hot-component column densities $N(\text{H}_2)_{\text{hot}}$ derived using the fiducial model, are in the range $0.01 \lesssim \langle \tau_\nu \rangle_{8-13 \mu\text{m}} \lesssim 0.1$, suggesting that the MIR emission from hot dust is indeed optically thin in these regions. Similar values for the optical depths at 11.7 μm were derived by De Buizer et al. (2005) from the MIR flux densities of their sample of massive star-forming regions, which are mostly $\lesssim 0.3$. Hence, we also investigated the changes produced by assuming that the MIR emission is optically thin, i.e., using

$$F_\nu = A \sigma_\nu B_\nu(T_d) e^{-\sigma_\nu N(\text{H}_2)_{\text{cold}}/2}, \quad (4)$$

where $A = N(\text{H}_2)_{\text{hot}} \Omega_d$. Note that here the parameters $N(\text{H}_2)_{\text{hot}}$ and Ω_d cannot be fitted simultaneously, but this allows us to avoid the constant-density condition (eq. [3]). Under this assumption we derived almost the same column densities $N(\text{H}_2)_{\text{cold}}$ and temperatures than those given by the fiducial model (differences $< 1\%$).

Since in all eight sources the MIR emission is located at the peak of the millimeter core, the fitted value of the cold dust cloud column density, $N(\text{H}_2)_{\text{cold}}$, can be compared with the column density, $N(\text{H}_2)_{1.2\text{mm}}$, derived from the peak value of the 1.2 mm flux density, $S_{1.2\text{mm}}^{\text{peak}}$ (Paper II). Assuming that the dust emission is optically thin at 1.2 mm, then

$$N(\text{H}_2)_{1.2\text{mm}} = \frac{S_{1.2\text{mm}}^{\text{peak}}}{\Omega_B B_{1.2\text{mm}}(T_c) \sigma_{1.2\text{mm}}}, \quad (5)$$

where Ω_B is the beam ($24''$) and T_c is the cold dust temperature derived in Section 4.1. We use $\kappa_{1.2\text{mm}} = 1 \text{ cm}^2 \text{ g}^{-1}$ from Ossenkopf & Henning (1994), since the effect of coagulation and presence of dirty ice mantles on dust grains in dense cold cores is likely to be important at this wavelength, where the Weingartner & Draine (2001) $R_V = 5.5$ model might not represent it properly (in particular, it ignores ice mantles). The column densities calculated using this relation are given in Column 5 of Table 4. The column densities derived from both methods are in good agreement, within a factor of $\simeq 2$, particularly considering the uncertainties inherent to both methods (e.g., in the opacities and dust-to-gas ratio), as well as the differences in angular resolution between the TIMMI2 and 1.2 mm observations.

4. DISCUSSION

4.1. Spectral Energy Distributions

We constructed SEDs for all the 18 sources of our survey, collecting the flux densities at 1.2 mm (SIMBA data, Paper II), at 12, 25, 60, and 100 μm (*IRAS* data), and at 8.3, 12.1, 14.7, and 21.3 μm , computed from the images of the *Midcourse Space Experiment (MSX)* Survey of the Galactic Plane (Price et al. 2001). We also included the *IRAC* (nonsaturated) and TIMMI2 F^{tot} fluxes listed in Tables 2 and 3, sum-

ming the flux of the two components for double sources. In most cases, a simple model consisting of emission from three uniform gray bodies with different temperatures and sizes was able to fit the SED. Since the regions exhibit generally complex MIR structures and probably present temperature gradients, this is indeed a coarse simplification. However, this model allows us to determine the average dust temperatures representative of each wavelength range.

The *MSX* fluxes were computed just over the corresponding compact sources in the *MSX* images, in order to reduce the effect of the different resolution ($\simeq 18''$) with respect to the *IRAC* data ($\simeq 1.8''$). Despite that difference, the SEDs show (Figure 6) that the *MSX* fluxes are consistent with the *IRAC* and TIMMI2 fluxes (see, e.g., the good correlation between *MSX* 8.3 μm fluxes and *IRAC* 8.0 μm fluxes), indicating that the major contribution to the ‘‘compact’’ *MSX* flux arises from the brightest source(s) within its beam. The *IRAS* data, however, have a much coarser resolution, so they include emission from a more extended region. Consequently, we often ignored the *IRAS* 12 μm flux for the fitting, and at 1.2 mm we considered the whole flux to make it representative of the same region that *IRAS* accounts. Conservative flux uncertainties of 20% were taken for SIMBA, *IRAS*, *MSX*, and *IRAC* data. For TIMMI2 data, we used the computed errors.

The model assumes the presence of three spherically symmetric components: a cold (c) extended component, a warm (w) inner component, and a hot (h) compact component. We consider them as radiating gray bodies and include the absorption of the radiation by the enclosing components. The total flux density is then given by,

$$F_\nu = F_\nu^h + F_\nu^w + F_\nu^c, \quad (6)$$

where

$$F_\nu^h = \Omega_h B_\nu(T_h) (1 - e^{-N_h \sigma_\nu}) e^{-(N_c + N_w) \sigma_\nu / 2} \quad (7)$$

$$F_\nu^w = \Omega_w B_\nu(T_w) (1 - e^{-N_w \sigma_\nu}) e^{-N_c \sigma_\nu / 2} \quad (8)$$

$$F_\nu^c = \Omega_c B_\nu(T_c) (1 - e^{-(\nu/\nu_0)^\beta}) \quad (9)$$

where the superscripts c, w, and h denote quantities for the cold, warm, and hot components, respectively; Ω is the solid angle; T the dust temperature, and N the H_2 column density. The cross section per hydrogen molecule, σ_ν , is given by Equation (2), where $R_{\text{dg}} = 1/125$ and $\mu = 2.8$, and we adopted the Weingartner & Draine (2001) $R_V = 5.5$ model for dust opacities (see Section 3.3). For the fit we considered as free parameters ν_0 , β , Ω_h , Ω_w , T_h , and T_w . The parameters of the cold component, T_c , Ω_c , and N_c were taken as fixed, and equal to the values listed in Paper II. Further, we adopted as upper limits for Ω_h and Ω_w , the values derived, respectively, from the *N*-band observations (Table 2) and *MSX E*-band observations. Because the column densities for the hot and warm components are small, the expression $(1 - e^{-N \sigma_\nu})$ acts as a linear term in N , producing degeneracy between the parameters N and Ω . To overcome this problem, we constrained the N_h and N_w parameters assuming constant density for all the temperature components, which implies $N_{h,w} = \sqrt{\Omega_{h,w} / \Omega_c} N_c$ for the hot and warm regions. Given the simplicity of the SED model and the differences in the data used, a more realistic density distribution is unnecessary.

Table 5 lists the parameters of the hot and warm components obtained from the best fit to the SED using the model described above. The FWHM angular sizes θ_h and θ_w were computed from the fitted solid angles assuming Gaussian emission

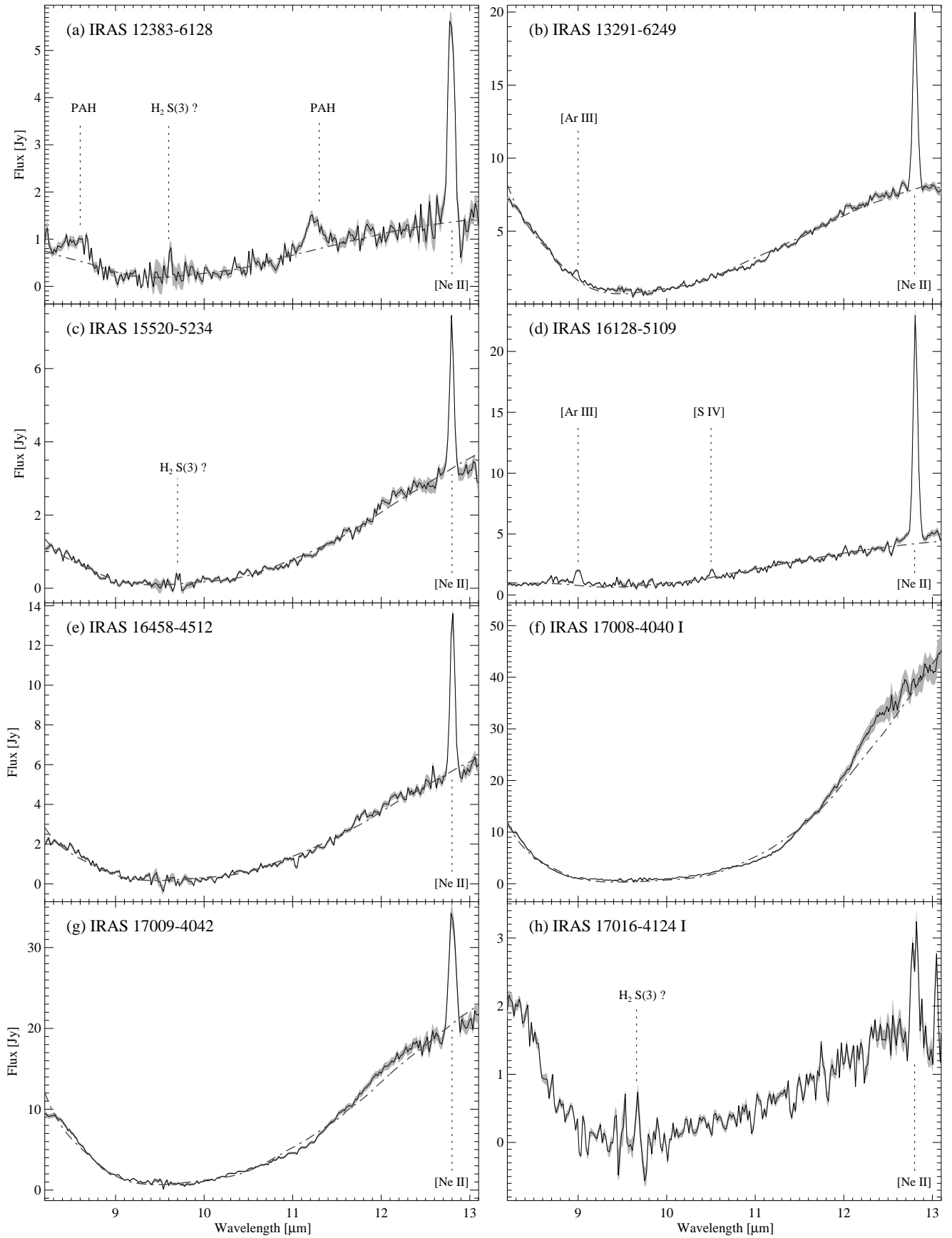


FIG. 5.— TIMMI2 8–13 μm spectra of the central parts of the sources. The statistical noise is shown as a filled region around the main curve. The spectral features found are labeled and marked with vertical dashed lines. We also show here the best fit model of the silicate absorption band (dashed curve) according to the procedure explained in Section 3.3.

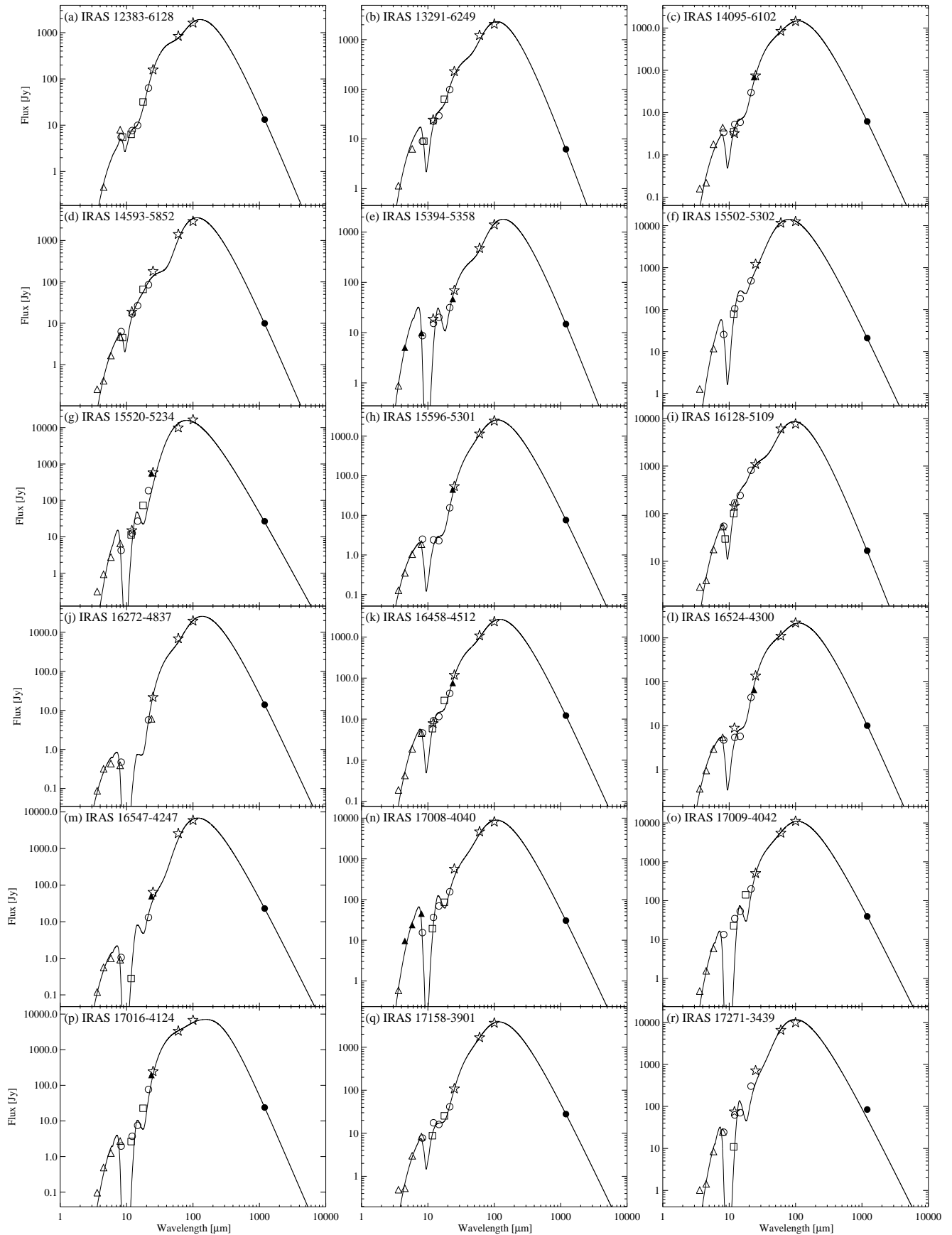


FIG. 6. — SEDs and their corresponding fits as described in Section 4.1. Flux symbols are a filled circle for 1.2 mm SIMBA, stars for *IRAS*, empty circles for *MSX*, squares for *TIMMI2*, and triangles for *Spitzer-IRAC/MIPS* (filled if they are saturated fluxes satisfying Equation (10)).

TABLE 5
PARAMETERS DERIVED FROM SED
FITTING

Source	T_h (K)	T_w (K)	θ_h ($''$)	θ_w ($''$)
12383–6128	361	71	0.43	12.3
13291–6249	398	93	0.34	3.9
14095–6102	342	65	0.26	7.2
14593–5852	328	117	0.41	2.9
15394–5358	432	99	0.46	2.8
15502–5302	263	103	1.78	6.6
15520–5234	276	112	1.17	2.7
15596–5301	420	63	0.16	7.2
16128–5109	323	123	1.02	5.8
16272–4837	591	75	0.09	4.1
16458–4512	330	73	0.38	6.7
16524–4300	425	68	0.27	9.0
16547–4247	504	139	0.15	1.5
17008–4040	340	98	1.12	6.2
17009–4042	400 ^a	132	0.57	5.2
17016–4124	400 ^a	96	0.33	6.1
17158–3901	331	62	0.49	12.0
17271–3439	332	181	1.18	3.7

NOTE. — Best fit parameters, see Equations (7) and (8). Solid angles (Ω) were converted to FWHMs (θ) assuming Gaussian distributions. Statistical errors are about 5%, 15%, 12%, and 30% for T_h , T_w , θ_h , and θ_w , respectively.

^a Unstable fitting; reached upper limit of 400 K.

distributions ($\Omega = 1.133 \times \theta^2$). Covariance-matrix errors are about 5%, 15%, 12%, and 30% for T_h , T_w , θ_h , and θ_w , respectively, but they could be underestimated. Most of the hot dust temperatures fall in the range $\simeq 250$ –450 K, whereas warm dust temperatures fall in the range $\simeq 60$ –150 K.

Figure 6 shows the SEDs and their corresponding fits for all sources. In most cases the fit is excellent. For the objects with the largest cold cloud column densities ($N_c > 3 \times 10^{23} \text{ cm}^{-2}$), which gives rise to a very deep silicate absorption feature at $\simeq 10 \mu\text{m}$ (e.g., IRAS 17271–3439, Figure 6(r)), the inclusion of absorption in the model in the MIR range became difficult. Because of this, particularly unstable fits were obtained for IRAS 17009–4042 and 17016–4124 (Figures 6(o) and (p), respectively). Hence, for these objects we set an upper limit of 400 K for T_h in order to obtain reasonable output parameters. The SEDs of the sources IRAS 16272–4837 and 16547–4247 (Figures 6(j) and (m)) exhibit a peculiar tendency in the IRAC fluxes, resulting in high hot-dust temperatures (591 K and 504 K, respectively). In these sources, the IRAC 4.5 μm flux density is similar (only slightly lower) to the 5.8 μm flux, which is higher than the 8.0 μm flux. This trend is consistent with the high absorption and the green fuzzies found in these regions.

For each source, the best-fit SED model was used as a validity check for the saturated IRAC/MIPS fluxes, which were recovered by applying the *imageworks* code (see Section 3.2), but were not used by the SED fitting. We list in Table 3, and show in Figure 6 as filled triangles, only those saturated fluxes that satisfy the condition

$$\left(\frac{F_{\lambda_0}^{\text{sat}} - F_{\lambda_0}^{\text{model}}}{\Delta F_{\lambda_0}} \right)^2 \leq \frac{1}{N} \sum_{i=1}^N \left(\frac{F_{\lambda_i} - F_{\lambda_i}^{\text{model}}}{\Delta F_{\lambda_i}} \right)^2, \quad (10)$$

where $F_{\lambda_0}^{\text{sat}}$ is the recovered flux at the saturated wavelength

$\lambda_0 = 4.5, 5.8, 8.0,$ or $24 \mu\text{m}$, $F_{\lambda}^{\text{model}}$ is the flux density given by the SED model, N is the number of data points being fitted, $\{F_{\lambda_i}\}$ are the observed fluxes, and ΔF_{λ} represents the corresponding error (it was taken as 30% for the saturated flux). In other words, we request that $F_{\lambda_0}^{\text{sat}}$ did not deviate from the SED model more than the χ^2 -per-data point value of the fit. Using this criterion, it was found that the *imageworks* tool had about 50% of success for embedded sources (e.g., seven out of 16 sources with saturated MIPS data).

4.2. Warm Dust Regions and Association with Ionized Gas

The high correlation between the spatial distribution of the MIR and radio emissions may suggest that the MIR emission is due to the ionized gas. However, extrapolating the observed radio continuum flux of the optically thin H II regions (Paper I) to the MIR, assuming a $\nu^{-0.1}$ frequency dependence, we find that the free-free emission at MIR wavelengths is negligible in comparison to the observed MIR fluxes (less than $\simeq 6\%$ at 8.0, 11.7, and 17.7 μm). We conclude that the MIR emission is tracing warm dust, located either within the H II region or in a thin shell around it. Kraemer et al. (2003) already found well-correlated MIR and radio distributions, and discarded the possibility that the emitting dust is distributed in a thin shell, since in that case the MIR emission would show evidence of limb-brightened morphology, which was not observed. None of the regions of our sample exhibit limb-brightened MIR emission.

We conclude that the MIR emission of the sources associated with radio-continuum emission arises from warm dust mixed with the ionized gas inside the H II region. Although dust grains and gas particles are likely to be dynamically coupled in H II regions, the heating of the dust grains is dominated by the UV radiation from the exciting source(s) and the ionized nebula, and not by the collisional exchange of energy with the gas (see, e.g., Spitzer 1978). This makes possible the coexistence of a plasma with a kinetic temperature of $\simeq 7000$ K and solid particles with a temperature of $\simeq 250$ –450 K (Section 4.1). These dust temperatures are consistent with the models by Natta & Panagia (1976) for dusty H II regions.

4.3. PAH Emission

The N -band TIMMI2 images (and probably the Q -band images too) are sensitive mainly to the emission of warm dust intimately associated with the ionized gas, or close to the exciting sources when there is no radio emission. They do not trace the presence of PAH, as indicated by the 8–13 μm spectroscopy toward seven of the eight sources of our sample (all but IRAS 12383–6128), where the emission bands in this wavelength range (the more prominent at 8.6 and 11.3 μm) are not seen.

Within the H II region or very close to a massive protostar, hard UV radiation destroys these molecules. For example, Povich et al. (2007) calculated the photodestruction rate of PAHs by extreme-UV (EUV) photons and found that this destruction mechanism accounts for the absence of PAHs in the M17 H II region. Because this region is one of the most energetic in the Galaxy, we expect that for the UC sources of our sample, the PAH destruction edge is located much closer to the exciting star(s). IRAS 12383–6128, which is the only one that presents PAH emission bands at 8.6 and 11.3 μm , has probably a softer UV spectrum than the others.

It is possible that a part of the outer diffuse emission ob-

served in the TIMMI2 images is due to PAHs, but since the slit was centered in the bright compact MIR sources, the PAH radiation was not strong enough to be detected. This explanation is supported by other MIR-spectroscopic observations found in the literature, with larger apertures, toward some of our sources, in which PAH emission is detected. In particular, the *IRAS* LSR spectrum (aperture of $6' \times 5'$) of IRAS 13291–6249 (Jourdain de Muizon et al. 1990) and the ISO spectrum (aperture of $14'' \times 20''$ in the wavelength range of TIMMI2) of IRAS 16128–5109 (Peeters et al. 2002) reveal the presence of PAH emission bands within the wavelength range of the TIMMI2 spectra (at 8.6 and $11.3 \mu\text{m}$). For IRAS 16128–5109, the PAH bands at 3.3, 6.2, 7.7, and $12.7 \mu\text{m}$ are also present (Peeters et al. 2002). PAH emission was also detected toward other sources of our sample which were not observed spectroscopically by us: IRAS 14593–5852 (IRAS LSR, Zavagno et al. 1992), IRAS 15502–5302 (ISO, Peeters et al. 2002), IRAS 15596–5301, and IRAS 17271–3439 (IRAS LSR, Jourdain de Muizon et al. 1990).

The latter result strongly suggests that the extended diffuse emission seen in most regions by the *Spitzer*–IRAC images beyond the radio continuum contours include an important contribution of PAH emission bands. The [3.6], [5.8], and [8.0] IRAC filters cover the PAH features at 3.3, 6.2, and $7.7 \mu\text{m}$, respectively. The [8.0] filter also covers the PAH band at $8.6 \mu\text{m}$. This extended diffuse emission is, however, more clearly seen in the [5.8] and [8.0] IRAC images than in the [3.6] images. A possible explanation (Povich et al. 2007) is that the $6.2 \mu\text{m}$ feature might have a greater fractional contribution to the [5.8] filter than the $3.3 \mu\text{m}$ band to the [3.6] filter (and the same for the [8.0] and [3.6] filters), or simply that the $3.3 \mu\text{m}$ band is intrinsically fainter. As for the TIMMI2 images, the *Spitzer* MIR emission at the location of the UC H II regions is more likely to correspond to warm dust continuum radiation with little or any contribution of PAH features.

4.4. High-Mass Protostellar Objects

The high angular resolution MIR observations presented here revealed the presence of bright compact MIR sources in the vicinity of, but not coincident with, UC H II regions, which are likely to signpost HMPOs. We identify a total of five new HMPO candidates within the regions observed with TIMMI2: IRAS 14593–5852 II (only detected at $17.7 \mu\text{m}$, see Figure 3), 17008–4040 I and II (Figure 4), 17016–4124 II (Figure 2(d)), and the compact component of IRAS 17158–3901 (Figure 2(e)).

In order to estimate the spectral types of these HMPO candidates, we derived MIR luminosities from the measured *N*- and *Q*-band fluxes, following a method based on the work by De Buizer et al. (2000). This technique provides good lower limits to the true bolometric luminosities of the stellar sources (see De Buizer et al. 2002). We note that estimates made using the *IRAS* fluxes are inappropriate since they include the contribution from the exciting star(s) of the nearby UC H II regions, as well as from other IR sources within the large *IRAS* beam. First, a dust color temperature is computed assuming that the MIR emission from warm dust is optically thin, as we suggested in Section 3.3. Our SED fits are also consistent with optically thin emission from the hot-dust component (using the derived N_h , the optical depths at $10 \mu\text{m}$ are in the range $\simeq 0.01 - 0.3$). We adopt a standard expression for the

TABLE 6
CHARACTERISTICS OF THE NEW HMPO
CANDIDATES

Source	T_{color} (K)	L_{MIR} (L_{\odot})	Spectral Type
14593–5852 II ^a	142	54500	O8.5
17008–4040 I	219	40900	O9.5
17008–4040 II	199	2490	B2
17016–4124 II	170	6120	B1
17158–3901	169	542	... ^b

NOTE. — Parameters T_{color} and L_{MIR} were computed from the observed *N*- and *Q*-band fluxes. The spectral types were derived from L_{MIR} (and thus are lower limits) and the calibration of Panagia (1973).

^a Lower limit *N*-band flux used.

^b Spectral type later than B3.

flux density (analog to Equation (4)):

$$F_{\nu} = A\sigma_{\nu}B_{\nu}(T_{\text{color}})e^{-N_c\sigma_{\nu}/2} . \quad (11)$$

Here, the factor $A = N_h\Omega$ is constant, σ_{ν} is given by Equation (2), and N_c by Equation (5), but truncated to the maximum column density derived from TIMMI2 spectra if it is higher than that value ($17.1 \times 10^{22} \text{ cm}^{-2}$, see Table 4), in order to moderate the effect of dust absorption (see below). The color temperature T_{color} is derived from the ratio of the integrated fluxes at the *N*- and *Q*-band (lower limit *N*-band flux for IRAS 14593–5852 II):

$$\frac{e^{hc/(k\lambda_2 T_{\text{color}})} - 1}{e^{hc/(k\lambda_1 T_{\text{color}})} - 1} = \frac{F_{\nu_1}}{F_{\nu_2}} \left(\frac{\lambda_1}{\lambda_2} \right)^3 \frac{\kappa_{\nu_2}}{\kappa_{\nu_1}} e^{-N_c(\sigma_{\nu_2} - \sigma_{\nu_1})/2} . \quad (12)$$

The MIR luminosity is then obtained integrating an expression of the form $F_{\nu} = A\sigma_{\nu}B_{\nu}(T_{\text{color}})$ from 1 to $1000 \mu\text{m}$ using the kinematical distance and the factor A to scale the flux density to the observed ones. Columns 2 and 3 of Table 6 give the computed color temperatures T_{color} and MIR luminosities L_{MIR} , respectively. We find that the derived spectral types, using the calibration of Panagia (1973) and the MIR luminosities, are earlier than B3 for four of our HMPO candidates (Column 4 of Table 6).

The spectral types derived by us are earlier than the typical spectral types obtained by De Buizer et al. (2000) using a similar method. A substantial difference between our technique and theirs is that we have considered the absorption of a cold cloud to model the observed fluxes, and corrected by extinction when computing the MIR luminosities. We found, however, that the employed method is quite sensitive to assumed column density N_c of the absorbing cloud, and therefore, in order to obtain strict lower limits for the spectral types, we recomputed the MIR luminosities under the assumption that there is no extinction ($N_c = 0$). This results now in two sources earlier than B3, namely, B0 for IRAS 14593–5852 II and B2 for 17008–4040 I, which thus might be considered as genuine HMPOs.

Figures 3 and 4 present the whole set of MIR images for the regions containing the two bona fide O-type high-mass protostar candidates: IRAS 14593–5852 II and 17008–4040 I. The *Spitzer*–IRAC images toward IRAS 14593–5852 (Figure 3(a)) show only diffuse emission toward the HMPO, bright in red ($8.0 \mu\text{m}$) and thus probably corresponding to the environment’s PAH emission, which dominates the large-scale structure. IRAS 14593–5852 II is then likely to be a

deeply embedded object. IRAS 17008–4040 I is bright in all available MIR images, even saturated in the IRAC filters (Figure 4(a)). The H II region is displaced by $\simeq 30''$ to the west of the TIMMI2 sources and associated with extended diffuse emission at $8.0 \mu\text{m}$. In addition to its high MIR luminosity and the lack of a detectable H II region (as indicated by the lack of both radio continuum emission and of the [Ne II] line in its *N*-band spectrum), there is additional evidence supporting the nature of IRAS 17008–4040 I as a high-mass protostar: (i) the *Spitzer*–IRAC image shows the presence of extended filamentary green fuzzies (see Section 3.2) to its northeast, suggesting outflowing activity; (ii) it is located at the center of a massive and dense molecular core (peak of 1.2 mm emission, Paper II), as predicted by all the massive star formation theories; and (iii) it is associated with different types of maser emission (Figure 4(b)), all of which are known to be associated with high-mass star-forming regions: OH masers at 1665/1667 MHz (e.g., Forster & Caswell 1989; Caswell 1998) and 6.7 GHz methanol masers (e.g., Walsh et al. 1998) just coincident with the position of IRAS 17008–4040 I, and water vapor maser emission at 22 GHz located $\simeq 4''$ to its southeast (Forster & Caswell 1989). In particular, 6.7 GHz methanol masers are only detected toward high-mass star-forming regions (Minier et al. 2003).

Finally, although the MIR luminosities given in Table 6 should only be considered as rough estimates, it is interesting to know where the HMPO candidates are located in the $L_{\text{bol}} - M_{\text{env}}$ (bolometric luminosity - envelope mass) diagram presented in the work of Molinari et al. (2008, their Figure 9). They successfully used it to follow the pre-main-sequence evolution of massive young stellar objects, by classifying a numerous sample of objects according to SED modeling and then comparing with the predictions of the turbulent core model (McKee & Tan 2003). We can do such exercise only for IRAS 17008–4040 I, since it is the only HMPO candidate that is far enough from nearby UC H II regions and thus the mass of the associated 1.2 mm core can be considered as its envelope mass (neglecting also the secondary object IRAS 17008–4040 II, which is much less luminous). Then, assuming $L_{\text{bol}} = 40900 L_{\odot}$ (MIR luminosity) and $M_{\text{env}} = 1200 M_{\odot}$ (Paper II), IRAS 17008–4040 I lies in a zone dominated by MM-P objects, below that occupied by IR-P objects in the notation of Molinari et al. (2008). They suggested that the IR-P stage may correspond to the arrival of the protostar on the zero-age main sequence (ZAMS), and the MM-P objects represent an earlier stage. The location of IRAS 17008–4040 I in the $L_{\text{bol}} - M_{\text{env}}$ plot would then categorize it as a pre-ZAMS object.

5. SUMMARY AND CONCLUSIONS

We present MIR *N*- and *Q*-band imaging, made with the TIMMI2 camera, toward 14 luminous *IRAS* point sources

with colors of UC H II regions, thought to be massive star-forming regions in early stages of evolution. We also present *N*-band spectroscopic observations toward eight of these regions. Images from the *Spitzer* legacy programs GLIMPSE and MIPS GAL for the 18 sources of our multiwavelength survey complement our data set. The main results and conclusions presented in this paper are summarized as follows.

The morphology of the TIMMI2 emission toward most regions (10) is simple, exhibiting either one (seven cases) or two (three cases) compact components each surrounded by extended emission. The compact components have physical sizes in the range 0.008–0.18 pc. The *Spitzer*–GLIMPSE images of these regions show even more extended diffuse emission than that seen by TIMMI2, most likely due to emission from PAH bands.

We find that the MIR emission traced by TIMMI2 corresponds to optically thin radiation from hot dust. The hot-dust temperatures, derived from fitting the SEDs, are typically $\simeq 250 - 450$ K.

We find that the spatial distribution of the MIR emission and radio continuum emission (Paper I) are highly correlated, suggesting that the ionized gas (radio source) and hot dust (MIR source) are intimately associated. We conclude that the emitting dust is located inside the H II region, mixed with the ionized gas. The *N*-band spectra toward seven of the eight sources exhibit bright [Ne II] line emission, consistent with the association of these sources with ionized gas.

The *N*-band spectra show, for all eight observed sources, the presence of a broad and deep silicate absorption band at $9.7 \mu\text{m}$, confirming their nature of deeply embedded objects within massive dense cores of cold dust and molecular gas. The H_2 column densities derived from this absorption feature are in the range $(7 - 17) \times 10^{22} \text{cm}^{-2}$, and are in good agreement (within a factor of $\simeq 2$) with those estimated from 1.2 mm data (Paper II). Only toward one source, IRAS 12383–6128, we detected the presence of PAH emission at 8.6 and $11.3 \mu\text{m}$. The lack of PAH emission in the spectra, with a small aperture and centered in the bright compact object, from the remaining sources is likely due to the presence of a hard radiation field which destroys these molecules in their neighborhood.

We discovered five bright compact MIR sources which are not associated with radio continuum emission, and are thus prime candidates for hosting young massive protostars. In particular, objects IRAS 14593–5852 II (only detected at $17.7 \mu\text{m}$) and 17008–4040 I are likely to be genuine O-type protostellar objects.

E.F.E.M., D.M., G.G., K.J.B., and J.E.P. gratefully acknowledge support from the Chilean Centro de Astrofísica FONDAF No. 15010003 and Proyecto BASAL PFB-06.

REFERENCES

- Benjamin, R. A. et al. 2003, *PASP*, 115, 953
 Beuther, H., Churchwell, E. B., McKee, C. F., & Tan, J. C. 2007, in *Protostars and Planets V*, ed. B. Reipurth, D. Jewitt, & K. Keil, 165–180
 Beuther, H., Sridharan, T. K., & Saito, M. 2005, *ApJ*, 634, L185
 Bonnell, I. A. & Bate, M. R. 2002, *MNRAS*, 336, 659
 Bonnell, I. A., Bate, M. R., & Zinnecker, H. 1998, *MNRAS*, 298, 93
 Bonnell, I. A., Vine, S. G., & Bate, M. R. 2004, *MNRAS*, 349, 735
 Bronfman, L., Nyman, L.-A., & May, J. 1996, *A&AS*, 115, 81
 Brooks, K. J., Garay, G., Mardones, D., & Bronfman, L. 2003, *ApJ*, 594, L131
 Carey, S. J. et al. 2009, *PASP*, 121, 76
 Caswell, J. L. 1998, *MNRAS*, 297, 215
 Chapman, N. L., Mundy, L. G., Lai, S.-P., & Evans, N. J. 2009, *ApJ*, 690, 496
 Cohen, M., Walker, R. G., Carter, B., Hammersley, P., Kidger, M., & Noguchi, K. 1999, *AJ*, 117, 1864
 De Buizer, J. M., Piña, R. K., & Telesco, C. M. 2000, *ApJS*, 130, 437
 De Buizer, J. M., Radomski, J. T., Piña, R. K., & Telesco, C. M. 2002, *ApJ*, 580, 305
 De Buizer, J. M., Radomski, J. T., Telesco, C. M., & Piña, R. K. 2005, *ApJS*, 156, 179
 Draine, B. T. 2003, *ARA&A*, 41, 241

- Engelbracht, C. W. et al. 2007, *PASP*, 119, 994
- Faúndez, S., Bronfman, L., Garay, G., Chini, R., Nyman, L.-Å., & May, J. 2004, *A&A*, 426, 97
- Fazio, G. G. et al. 2004, *ApJS*, 154, 10
- Forster, J. R. & Caswell, J. L. 1989, *A&A*, 213, 339
- Garay, G., Brooks, K. J., Mardones, D., & Norris, R. P. 2006, *ApJ*, 651, 914, (Paper I)
- Garay, G. & Lizano, S. 1999, *PASP*, 111, 1049
- Garay, G., Mardones, D., Brooks, K. J., Videla, L., & Contreras, Y. 2007, *ApJ*, 666, 309, (Paper II)
- Horne, K. 1986, *PASP*, 98, 609
- Jourdain de Muizon, M., Cox, P., & Lequeux, J. 1990, *A&AS*, 83, 337
- Kraemer, K. E. et al. 2003, *ApJ*, 588, 918
- Krumholz, M. R., Klein, R. I., & McKee, C. F. 2007, *ApJ*, 656, 959
- Mardones, D. 1998, Ph.D. Thesis, Harvard Univ.
- McKee, C. F. & Tan, J. C. 2003, *ApJ*, 585, 850
- Meade, M. R. et al. 2005, *GLIMPSE Legacy Science Data Products (ver 1.5; Madison: Dept. Astron., Univ. Wisconsin)*
- Minier, V., Ellingsen, S. P., Norris, R. P., & Booth, R. S. 2003, *A&A*, 403, 1095
- Molinari, S., Pezzuto, S., Cesaroni, R., Brand, J., Faustini, F., & Testi, L. 2008, *A&A*, 481, 345
- Morris, P. W., Noriega-Crespo, A., Marleau, F. R., Teplitz, H. I., Uchida, K. I., & Armus, L. 2004, *ApJS*, 154, 339
- Natta, A. & Panagia, N. 1976, *A&A*, 50, 191
- Noriega-Crespo, A. et al. 2004, *ApJS*, 154, 352
- Ossenkopf, V. & Henning, T. 1994, *A&A*, 291, 943
- Panagia, N. 1973, *AJ*, 78, 929
- Pascucci, I., Apai, D., Henning, T., Stecklum, B., & Brandl, B. 2004, *A&A*, 426, 523
- Peeters, E. et al. 2002, *A&A*, 381, 571
- Povich, M. S. et al. 2007, *ApJ*, 660, 346
- Price, S. D., Egan, M. P., Carey, S. J., Mizuno, D. R., & Kuchar, T. A. 2001, *AJ*, 121, 2819
- Rathborne, J. M., Jackson, J. M., Chambers, E. T., Simon, R., Shipman, R., & Frieswijk, W. 2005, *ApJ*, 630, L181
- Reimann, H.-G., Linz, H., Wagner, R., Relke, H., Kaeufl, H. U., Dietzsch, E., Sperl, M., & Hron, J. 2000, in *Proc. SPIE Vol. 4008, Optical and IR Telescope Instrumentation and Detectors*, ed. M. Iye & A. F. Moorwood, 1132–1143
- Rieke, G. H. et al. 2004, *ApJS*, 154, 25
- Saviane, I. & Doublier, V. 2005, *La Silla-Paranal Observatory. TIMMI2: User Manual (Issue 1.0; ESO)*
- Siebenmorgen, R., Krügel, E., & Spoon, H. W. W. 2004, *A&A*, 414, 123
- Smith, H. A., Hora, J. L., Marengo, M., & Pipher, J. L. 2006, *ApJ*, 645, 1264
- Smith, M. D. & Rosen, A. 2005, *MNRAS*, 357, 1370
- Spitzer, L. 1978, *Physical Processes in the Interstellar Medium (New York Wiley-Interscience, 1978. 333 p.)*
- Walsh, A. J., Burton, M. G., Hyland, A. R., & Robinson, G. 1998, *MNRAS*, 301, 640
- Weingartner, J. C. & Draine, B. T. 2001, *ApJ*, 548, 296
- Werner, M. W. et al. 2004, *ApJS*, 154, 1
- Wood, D. O. S. & Churchwell, E. 1989, *ApJ*, 340, 265
- Zavagno, A., Cox, P., & Baluteau, J.-P. 1992, *A&A*, 259, 241